Spectral properties of $LiTaO_3:Pr^{3+}$ under high hydrostatic pressure

2005 J. Phys.: Condens. Matter 17 5381

(http://iopscience.iop.org/0953-8984/17/35/006)

INSTITUTE OF PHYSICS PUBLISHING JOURNAL OF PHYSICS: CONDENSED MATTER

J. Phys.: Condens. Matter **17** (2005) 5381–5395 doi:10.1088/0953-8984/17/35/006

Spectral properties of $LiTaO_3$:Pr^{3+} under high hydrostatic pressure

W Gryk[1], D Dyl[1], W Ryba-Romanowski[2] and M Grinberg[1]

[1] Institute of Experimental Physics, University of Gdańsk, Wita Stwosza 57, 80-952 Gdańsk, Poland
[2] Institute of Low Temperature and Structural Research, Polish Academy of Sciences, Okólna 2, 50-422 Wrocław, Poland

Received 20 April 2005, in final form 28 July 2005
Published 19 August 2005
Online at stacks.iop.org/JPhysCM/17/5381

Abstract

The high-pressure photoluminescence of the $LiTaO_3$:Pr^{3+} system obtained for the pressure range from ambient to 232 kbar at 20 K and ambient temperatures is presented. The observed pressure red shift of all spectral lines representing the f–f transitions is related to the changes in F^2 Racach integral and the spin–orbit coupling with pressure. To analyse the deexcitation kinetics and the dependence of the intensity of the $^3P_0 \rightarrow {}^3H_4$ and $^1D_2 \rightarrow {}^3H_4$ on the excitation wavelength and pressure we propose a model of a Pr^{3+} trapped exciton with a hole localized at the Pr^{3+} and an electron at the Rydberg states bounded by the long-range Coulomb potential of the hole.

1. Introduction

$LiTaO_3$ and $LiNbO_3$ doped with transition metal and rare earth ions have been extensively investigated since the discovery of $LiNbO_3$ in 1949 [1]. In ambient conditions, both crystals are ferroelectrics. The ferroelectric–paraelectric transition temperatures are 1480 K for $LiNbO_3$ and 950 K for $LiTaO_3$ [2]. Both crystals belong to the $R3c$ space group and have large electro-optic and nonlinear coefficients [3, 4]. The interest in $LiTaO_3$ and $LiNbO_3$ has grown significantly, as the crystals can offer a nonlinear effect and lasing ability simultaneously. $LiNbO_3$ has been doped with Er^{3+} [5], Tm^{3+} [6, 7], Ho^{3+} [8], Nd^{3+} [9], Dy^{3+} [10, 11] and Pr^{3+} [12, 13]. Fewer papers have been devoted to the spectral properties of $LiTaO_3$ doped mainly with Nd^{3+} [14–18] and Pr^{3+} [19].

The main idea of doping materials with Pr^{3+} is related to the ability of Pr^{3+} for the generation of the broad band parity allowed blue, violet or UV emission [20, 21] related to the $4f^15d^1 \rightarrow 4f^2$ transition that competes with the transitions from state $^1S_0$ state [22, 23]. The other applications result from the possibility of photon cascade emission [24–26] after UV excitation. Nonlinearity of $LiNbO_3$ and $LiTaO_3$ crystals would also appear very likely in the case of doping with Pr^{3+}.

The basic optical spectroscopy of $LiNbO_3:Pr^{3+}$ and $LiTaO_3:Pr^{3+}$ has been already reported in the papers [12, 27, 13] and [19], respectively. In contrast to other perovskites, like $KMgF_3$, which is characterized by an energy of the fundamental band gap greater than 12 eV [28], the band gap of $LiNbO_3:Pr^{3+}$ and $LiTaO_3:Pr^{3+}$ is much narrower and is less than 4 eV [2]. As a result we can observe emission only from the lower excited states of Pr^{3+}; $^3P_0$ and $^1D_2$.

In $LiNbO_3:Pr^{3+}$, the intensity of the emission related to the $^3P_0 \rightarrow {}^3H_4$ transition is weaker than the emission related to $^1D_2 \rightarrow {}^3H_4$ [12, 13]. The multiphonon depopulation of the $^3P_0$ state to the $^1D_2$ state in $LiNbO_3:Pr^{3+}$ has been proposed [12]. Since in the case of $LiTaO_3:Pr^{3+}$ that is very similar to $LiNbO_3:Pr^{3+}$, the emission related to the $^3P_0 \rightarrow {}^3H_4$ transition is much more intensive than that related to the $^1D_2 \rightarrow {}^3H_4$ transition [19], we have considered that the multiphonon process cannot be the only process responsible for the nonradiative $^3P_0 \rightarrow {}^1D_2$ transition. The other possibility is the nonradiative deexcitation of the $^3P_0$ state through the Pr^{3+} trapped exciton states [23, 29]. To verify this hypothesis we have measured the photoluminescence spectra of $LiNbO_3:Pr^{3+}$ at different high hydrostatic pressures and temperatures [30, 31]. We have shown that with increasing pressure the intensity of the yellow $^1D_2 \rightarrow {}^3H_4$ emission decreases and additional broad band luminescence in the IR region appears. We have attributed the IR emission to the recombination of the Pr^{3+} trapped exciton. The Pr^{3+} trapped exciton states are also seen in the $^1D_2 \rightarrow {}^3H_4$ luminescence excitation spectra [30]. Considering the pressure and temperature dependence of the intensity ratio of the broad band of the excito emission to the sharp lines of the $^1D_2 \rightarrow {}^3H_4$ emission in $LiNbO_3:Pr^{3+}$ system, we were able to estimate the energy of the trapped exciton state and its dependence on pressure [31, 32].

The damping of the $^1D_2 \rightarrow {}^3H_4$ emission with pressure observed in $LiNbO_3:Pr^{3+}$ is a result of the decrease of the energy of the trapped exciton state (with respect to energies of states belonging to the $4f^2$ electronic configuration) that stimulates the nonradiative depopulation of the $^1D_2$ state [31]. At ambient conditions the minimum energy of the electronic manifold representing the trapped exciton in $LiNbO_3:Pr^{3+}$ appears between the energy of the $^3P_0$ and $^1D_2$ states. The band gap energy of $LiTaO_3$ is equal to 4 eV [2], and is larger than the respective value for $LiNbO_3$, 3.1 eV [2]. One expects that the energy of the Pr^{3+} trapped exciton is higher in $LiTaO_3:Pr^{3+}$ than in $LiNbO_3:Pr^{3+}$ and therefore high-pressure spectroscopy of $LiTaO_3:Pr^{3+}$ will provide information on the nonradiative processes in the $^3P_0$ state, whose population can be controlled by pressure in the same way as the population of the $^1D_2$ state in $LiNbO_3:Pr^{3+}$ was [31].

In this paper we present ambient pressure absorption, emission and luminescence excitation spectra of $LiTaO_3:Pr^{3+}$. Special attention has been paid to the high-pressure photoluminescence of $LiTaO_3:Pr^{3+}$ for the pressure range from ambient to 232 kbar for temperatures from 20 K to ambient. We have analysed the pressure and temperature dependence of the energies of the $^3P_0 \rightarrow ({}^3H_4, {}^3H_5, {}^3H_6, {}^3F_3, {}^2F_2)$ and $^1D_2 \rightarrow ({}^3H_4, {}^3H_5, {}^3H_6, {}^3F_3)$ transitions and the pressure dependence of the intensity ratio of the $^3P_0 \rightarrow {}^3H_4$ to $^1D_2 \rightarrow {}^3H_4$ emission.

2. Experimental results

2.1. Sample preparation

A single crystal of praseodymium-doped lithium tantalate was grown from a congruent melt by the Czochralski method. The charge material was prepared with Li_2CO_3 and Ta_2O_5 substrates. The intended amount of Pr^{3+} admixture was introduced in the form of praseodymium oxide. Chemicals were mixed, pressed isostatically and heated in iridium crucible at 1100 °C for 3 h. The single crystal was grown in an inductively heated furnace equipped with an after-heater

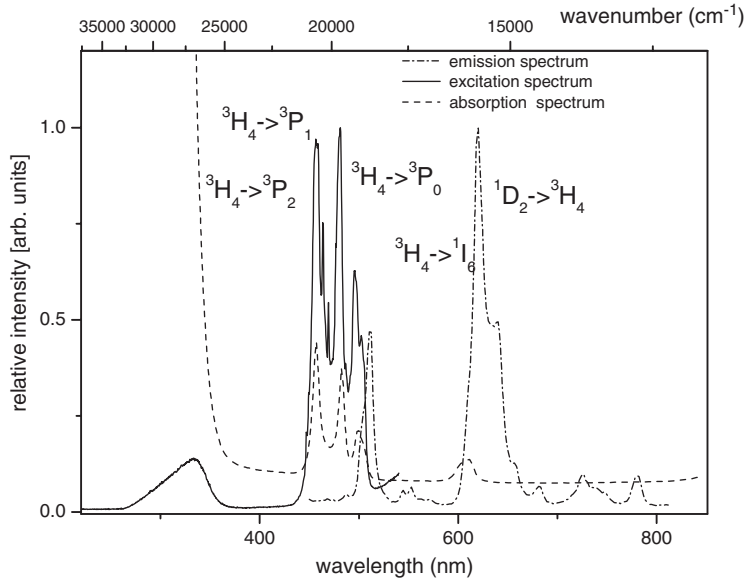

Figure 1. Ambient pressure and ambient temperature absorption, emission (excited with wavelength 325 nm) and luminescence excitation spectra of $LiTaO_3:Pr^{3+}$ (the luminescence was monitored at wavelength 622 nm).

to reduce the temperature gradient near the crystal–melt interface, thus diminishing crystal strains. The pulling rate was 5 mm h^{-1}, and the rotation rate was 40 rpm. The obtained crystal was annealed at 1400 °C and cooled down at the rate 30 °C h^{-1}. The concentration of Pr^{3+} ions estimated by chemical analysis was 0.4 mol%, which is equivalent to 1.27×10^{20} ions cm^{-3}.

2.2. Ambient-pressure spectroscopy

Absorption spectra were registered using a standard V–UV spectrophotometer 'SPECORD' (Carl Zeiss Jena). Photoluminescence spectra were measured under excitation of a He–Cd laser (325 nm) using a PGS2 spectrophotometer (Carl Zeiss Jena) working as an monochromator. Emission was detected by the photomultiplier (Hamamatsu, R943-02) working in the photon-counting regime. A closed cycle helium cryostat (Cryogenics Inc., DE-202) was used for all low-temperature measurements. Luminescence excitation spectra were measured with a 500 W xenon lamp, two SMP2 (Carl Zeiss Jena) monochromators and the photomultiplier R928.

Ambient pressure and temperature absorption spectra, luminescence spectra and luminescence excitation spectra monitored at 622 nm corresponding to the $^1D_2 \rightarrow {}^3H_4$ transition are presented in figure 1. In the absorption and luminescence excitation spectra the three bands related to transitions from the ground $^3H_4$ state to $^3P_0$, $^3P_1$ and $^3P_2$ excited states with energies 19 690, 20 530 and 21 700 cm^{-1}, respectively, are seen. In the absorption spectra we additionally see two bands (at 16 250 and 16 450 cm^{-1}) related to transitions from the ground state $^3H_4$ to the $^1D_2$ state.

The crystal-field splitting of the Pr^{3+} ion optically active $4f^2$ multiplets for cubic and C_{3V} symmetry is depicted symbolically in figure 2. From this diagram one can see for example that the ground state $^3H_4$ is split into $^3T_1$, $^3A_1$, $^3T_2$ and ^3E due to the cubic field and additionally into non-degenerated and doubly degenerated states labelled by the irreducible representations

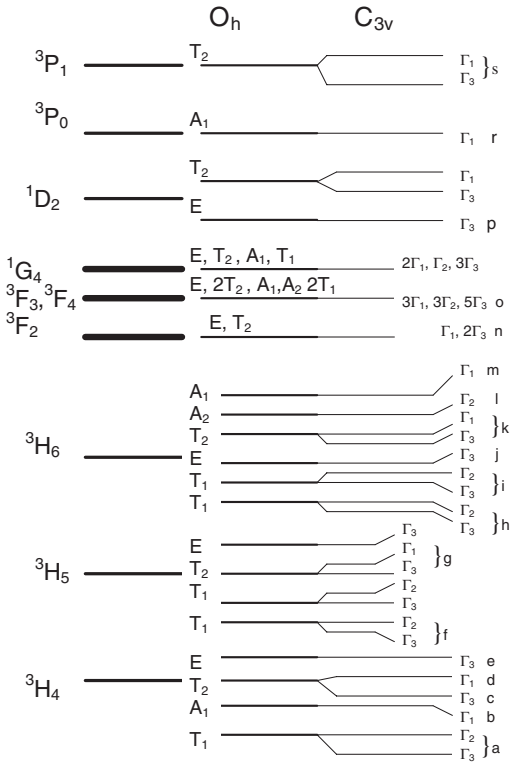

Figure 2. The crystal-field splitting scheme of the lowest $4f^2$ Pr^{3+} multiplets for cubic and C_{3V} symmetry.

Γ_1, Γ_2 and Γ_3, respectively, of the C_{3V} point group (Bethe notation). The lowest cubic field state, $^3T_1(^3H_4)$, splits into Γ_3, Γ_2 components which are not resolved in our measurements and thus have a common label 'a' (see also table 1).

The fundamental absorption edge appears at energy 27 000 cm^{-1} (3.46 eV). Since it is smaller than the energy of the band gap it can be attributed to the ionization of the Pr^{3+} ion: ($Pr^{3+} \rightarrow Pr^{4+}$). In the excitation spectra for the energy just above the absorption edge we see the broad band peaked at 31 500 cm^{-1}, which can be attributed to the transition from the ground state $^3H_4$ to the Pr^{3+} trapped exciton state.

The emission spectra seen at 20 K and room temperature are presented in figures 3(a) and (b), respectively. Two dominating groups of lines correspond to the $^3P_0 \rightarrow {}^3H_4$ and $^1D_2 \rightarrow {}^3H_4$ transitions. All transitions we have observed are labelled in figures 3(a), (b) and are collected in table 1.

2.3. High-pressure photoluminescence spectra

High-pressure photoluminescence spectra were measured at pressures from ambient to 232 kbar at 20 K and room temperature. Pressure was applied in a diamond anvil cell (DAC) of type D04, designed and produced by Diacell Product Inc. Poly (dimethylsiloxane) oil was used as the pressure-transmitting medium, and a small piece of ruby crystal was used as a pressure detector. Photoluminescence was excited with a He–Cd laser (325 nm, 5 mW). The photoluminescence signal was dispersed using a PGS2 (Carl Zeiss Jena) spectrometer

Table 1. Ambient pressure energies and pressure shifts of the Pr^{3+} f–f emission lines. In the first column identifications of individual lines are presented.

Transitions (labels a–s as in figure 2)		Wavenumber (cm^{-1})	Pressure shift, K_i (cm^{-1} $kbar^{-1}$)
$^3P_0 \rightarrow {}^3H_4$	r → a	19 859	−2.45 ± 0.20
	r → c	19 664	−3.50 ± 0.30
	r → d	19 552	−2.75 ± 0.25
$^3P_1 \rightarrow {}^3H_5$	s → f	18 070	−2.40 ± 0.23
$^3P_0 \rightarrow {}^3H_5$	r → f	17 760	
	r → g	17 524	
$^1D_2 \rightarrow {}^3H_4$	p → a	16 190	−2.13 ± 0.05
	p → b	16 100	−2.31 ± 0.15
	p → e	15 733	−2.15 ± 0.15
$^3P_0 \rightarrow {}^3H_6$	r → h	15 650	−2.41 ± 0.05
$^3P_0 \rightarrow {}^3F_2$	r → n	15 322	−2.68 ± 0.17
$^3P_1 \rightarrow {}^3F_4, {}^3F_3$	s → o	14 935	−2.67 ± 0.15
$^1D_2 \rightarrow {}^3H_5$	p → f	14 016	−2.45 ± 0.07
	p → g	13 782	−2.61 ± 0.16
$^3P_0 \rightarrow {}^3F_4, {}^3F_3$	r → o	13 090	−2.71 ± 0.13
$^1D_2 \rightarrow {}^3H_6$	p → h	12 110	−2.41 ± 0.07
	p → i	11 979	−2.63 ± 0.08
	p → j	11 857	
	p → k	11 573	−2.29 ± 0.11
	p → l	11 407	−2.68 ± 0.12
	p → m	11 186	

working as an monochromator, and detected by a photomultiplier (Hamamatsu, R943-02) working in the photon-counting regime. The DAC was cooled using a closed cycle helium cryostat (Cryogenics Inc., DE-202).

The photoluminescence spectra obtained at 20 K at different pressures are presented in figure 4(a). The emission spectra obtained at ambient temperature are very similar. In figure 4(b) the pressure dependence of the specific emission peaks measured at 20 K is presented. One notices that the energies of the peaks depend linearly on pressure. The respective pressure shifts are listed in table 1.

For all pressures the dominating spectral lines correspond to the $^1D_2 \rightarrow {}^3H_4$ transition. The intensity of the $^3P_0 \rightarrow {}^3H_4$ transition is lower. At 20 K and room temperature one notices that the relative intensity of the $^3P_0 \rightarrow {}^3H_4$ emission decreases with increasing pressure and becomes very weak or negligible at pressures higher than 140 kbar. This relates to all transition from the $^3P_0$ state. Damping of the emission from the $^3P_0$ state is seen also in figure 5, where the relative intensity ratios of the $^3P_0 \rightarrow {}^3H_4$ to $^1D_2 \rightarrow {}^3H_4$ transitions versus pressure for 20 K and ambient temperature versus pressure are shown.

3. Analysis of the emission spectra in the framework of the crystal-field model

The dependencies of the energies of the sharp lines emission on pressure have been analysed using the standard perturbation approach. We assumed that the crystal-field Hamiltonian H_{CF} can be treated as a small perturbation of the free-ion Hamiltonian H_0. Thus the total

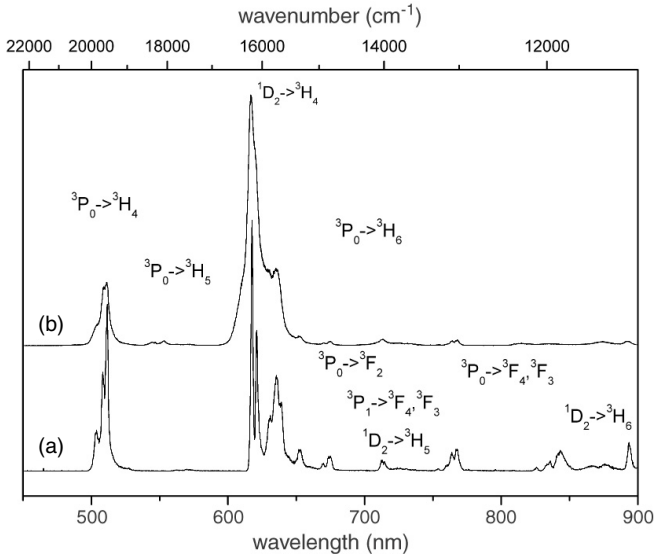

Figure 3. Ambient pressure emission spectra of $LiTaO_3:Pr^{3+}$ obtained at 20 K (a) and at room temperature (b).

Hamiltonian is

$$H = H_0 + H_{\mathrm{CF}}. \tag{1}$$

According to Judd and Crosswhite [33], the various interactions in the free-ion Hamiltonian can be factorized in their angular contributions and for the f^2 configuration the form of the H_0 is

$$H_0 = E_{\mathrm{AVE}} + \sum_{k=2,4,6} F^k f_k + \zeta_{4\mathrm{f}} A_{\mathrm{SO}} + \alpha L(L+1) + \beta G(G_2) + \gamma G(R_7) + \sum_{k=0,2,4} M^k m_k + \sum_{k=2,4,6} P^k p_k \tag{2}$$

where f_k, A_{SO} and m_k, p_k are operators representing angular contributions of the electrostatic, spin–orbit and magnetic interactions, respectively. $G(G_2)$ and $G(R_7)$ are the eigenvalues of the Casimir operators for the groups G_2 and R_7. L is the total angular momentum. The radial contributions described by the factors F^k, $\zeta_{4\mathrm{f}}$, α, β, γ, M^k, P^k are treated as adjustable parameters. In the calculations the F^4, F^6 parameters can be expressed approximately as a function of the F^2:$F^4 = 0.668\ F^2$, $F^6 = 0.495\ F^2$. Also the parameters M^k and P^k are mostly maintained by the ratios $M^2/M^0 = 0.56$, $M^4/M^0 = 0.38$ and $P^4/P^2 = 0.75$, $P^6/P^2 = 0.5$ [35].

The crystal-field Hamiltonian can be written in the terms of crystal-field parameters B_q^k as

$$H_{\mathrm{CF}} = \sum_{i,k,q} B_k^q\ C_q^{(k)}(\varphi_i, \theta_i) \tag{3}$$

where

$$C_q^{(k)}(\varphi_i, \theta_i) = \sqrt{\frac{4\pi}{2k+1}} Y_{kq}(\varphi_i, \theta_i) \tag{4}$$

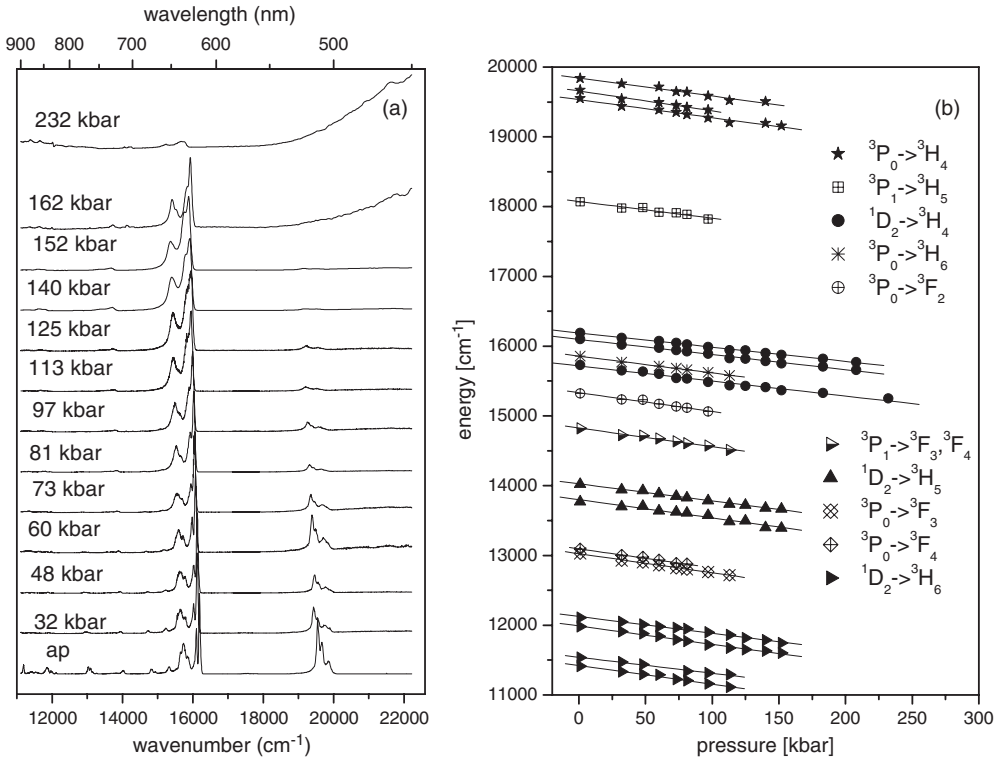

Figure 4. (a) Emission spectra of $LiTaO_3:Pr^{3+}$ obtained at 20 K at different pressures. (b) Position of the emission peaks versus pressure. All data apart from the $^3P_1 \rightarrow {}^3F_3, {}^3F_4$ transition, which was measured at room temperature, were obtained at 20 K.

are spherical tensor operators [34]. The sum over i covers the two electrons of the configuration $4f^2$ of Pr^{3+}. The crystal-field splitting is described only by the even part of H_{CF} (for the 'f' systems $k = 2, 4, 6$) and the values of q are limited by the point group of the crystal rare-earth site. In the energy level calculations the term $B_0^0 C_0^{(0)}$ is absorbed in the free-ion parameter E_{AVE} together with other spherically symmetric interactions.

The octahedrally coordinated sites in the $LiTaO_3$ and $LiNbO_3$ lattices have C_3 (near C_{3V}) symmetry. It is also known that $LiNbO_3$ and $LiTaO_3$ are very similar in their electronic structure [2]. On the other hand, as was shown in [36], the energy level calculations of $LiNbO_3:Pr^{3+}$ are not improved when using the actual C_3 symmetry instead of the approximated higher C_{3V} symmetry. Assuming that such an approximation is also valid for the $LiTaO_3:Pr^{3+}$ system, we may write the crystal-field Hamiltonian as [37]

$$H_{CF} = B_2^0 C_0^{(2)} + B_4^0 C_0^{(4)} + B_4^3 (C_3^{(4)} - C_{-3}^{(4)}) + B_6^0 C_0^{(6)} + B_6^3 (C_3^{(6)} - C_{-3}^{(6)}) + B_6^6 (C_6^{(6)} + C_{-6}^{(6)}). \quad (5)$$

It has been assumed that the Oz axis is parallel to the trigonal axis (quantization axis) and the Oy axis is parallel to the σ_v plane. Six real crystal-field parameters B_k^q and two free-ion parameters, F^2 and ζ_{4f}, were obtained by diagonalization of the total Hamiltonian including full J mixing and using a least squares fitting procedure that minimizes the differences between experimental and calculated energy level positions which correspond to the energies of radiative transitions ('a–s' levels from figure 2 and table 1). Such calculations were made for all

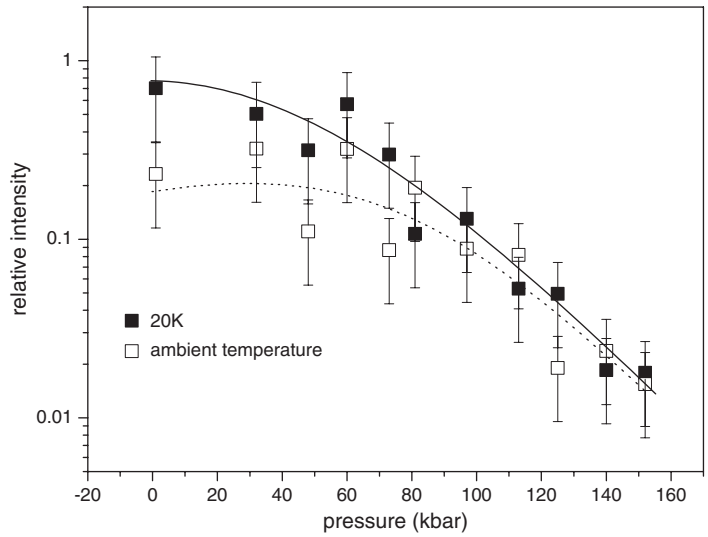

Figure 5. Relative intensity of the cumulative emission from the $^3P_0$ state ($^3P_0 \rightarrow {}^3H_4 + {}^3P_0 \rightarrow {}^3F_3, {}^3F_4$) to the cumulative emission from the $^1D_2$ state ($^1D_2 \rightarrow {}^3H_4, {}^3H_5, {}^3H_6$).

available pressure values. As initial values of the parameters (at ambient pressure) we used those determined by Carnall [39] (free-ion parameters also including α, β, γ, M^0, P^2) and Morrison [40, 41] (crystal-field parameters).

Due to the limited numbers of the observed lines (some of the crystal-field levels remain unresolved) and additional symmetry assumptions, the quality of the obtained results is not very high, and the difference between experimental and calculated levels is 48 cm^{-1}. However, it is good enough to obtain the pressure dependence of the free-ion and the crystal-field parameters.

To reproduce pressure changes in the emission spectra one described changes of Slater integral F^2 and spin–orbit coupling constant ζ_{4f} by the following equations:

$$F^2 = [65\,700 \pm 60 - (11.8 \pm 0.7)p]\ \mathrm{cm}^{-1} \tag{6}$$

and

$$\zeta_{4f} = [714 \pm 5 - (0.19 \pm 0.02)p]\ \mathrm{cm}^{-1} \tag{7}$$

for pressure p expressed in kbar in the range between ambient pressure and 250 kbar. A linear dependence on pressure could be simply understood—in a first-order approximation—as a result of decreasing ligand–ion distances under the influence of hydrostatic pressure.

To perform the calculations we used the experimentally obtained dependence of the emission peaks on pressure. To calculate the transition energy for a given pressure we used the relation

$$E_i(p) = E_{0i} + K_i p. \tag{8}$$

The slope values K_i and standard errors for the most interesting transitions are listed in table 1.

The obtained crystal-field parameters are listed in table 2. Although these parameters are of the same order as those obtained for $LiNbO_3$:Pr^{3+} (see [36]), there is a rather big discrepancy in values of the parameter B_2^0 and B_4^3 for these two systems even for ambient pressure. In spite of this fact one can see that the crystal-field parameters behave in a more complicated way on pressure than the free-atom parameters. Parameters B_2^0, B_4^q and B_6^0 change monotonically but

Table 2. Values of crystal-field parameters of Pr^{3+} in $LiTaO_3$ for various pressures. The coefficients are expressed in cm^{-1}.

p (kbar)	0	50	100	150	200
B_2^0	−270	−170	−105	−80	−91
B_4^0	−1100	−1220	−1370	−1520	−1890
B_4^3	126	98	30	27	29
B_6^0	−520	−400	−315	−305	−290
B_6^3	−187	−192	−174	−176	−183
B_6^6	−305	−270	−250	−285	−257

Table 3. Ratios of crystal-field parameters of Pr^{3+} in $LiTaO_3$ obtained for various pressures. In the last column the cubic ratios are presented.

p (kbar)	0	50	100	150	200	'Pure cubic'
B_4^3/B_4^0	−0.115	−0.080	−0.021	−0.018	−0.015	−1.195
B_6^3/B_6^6	0.36	0.48	0.55	0.58	0.63	0.60
B_6^6/B_6^0	0.59	0.67	0.79	0.93	0.89	0.63

B_6^3 and B_6^6 remain almost unchanged (within the error $= \pm 30\ cm^{-1}$). One should remember that these parameters are not only a function of ligand–ion distances but they also depend on the bonding characteristics and shape of the coordination polyhedron. In the case of $LiTaO_3$:Pr^{3+} crystal the values of the B_2^0 and B_4^q parameters depend strongly on the position of axial and equatorial ligands and on the displacement of Pr^{3+} along the ferroelectric axis. Considering the *point charge electrostatic model* of the crystal field [37], one notices that axial ligands cause an increase in the B_2^0 and B_4^0 parameters and a decrease in the B_6^0 parameter. In contrast, the existence of equatorial ligands causes an increase in the B_4^0 parameter and a decrease in the B_2^0 and B_6^0 parameters. In the case of pure cubic octahedral environment, the B_2^0 parameter should be equal to 0, and the 'cubic' ratios B_4^3/B_4^0, B_6^3/B_6^6, B_6^6/B_6^0 are $-\sqrt{10/7} \approx -1.195$, $\sqrt{210}/24 \approx 0.60$, $\sqrt{231}/24 \approx 0.63$, respectively [37]. The values of these ratios obtained for $LiTaO_3$:Pr^{3+} for different pressures are given in table 3. The values of B_6^3/B_6^6 and B_6^6/B_6^0 are close to their 'cubic' values. On the other hand one notices a large discrepancy between our value and the 'cubic' B_4^3/B_4^0 value, and also a huge absolute value of B_2^0 that decreases with p. Considering the superposition model [37, 38], one notices that the coefficients B_k^q depend on the positions of the ligands defined by the distance from the central ion, R_L, and on angles θ_L and ϕ_L, according to the formula

$$B_k^q = \sum_L \frac{\overline{A}_k(R_L)}{\lambda_{k,q}} G_{kq}(\theta_L, \phi_L) \tag{9}$$

where the coefficients $\overline{A}_k(R_L)$ can be presented as the following integrals:

$$\overline{A}_k(R_L) = \int \frac{\rho(R_L) r^k}{R_L^{k+1}} \mathrm{d}\tau, \tag{10}$$

and $G_{kq}(\theta_L, \phi_L)$ are functions depending on angles θ_L and ϕ_L, and $\lambda_{k,q}$ are constants. In the first approximation when pressure would change only the central-ion–ligand distances the ratios B_4^3/B_4^0, B_6^6/B_6^0 and B_6^3/B_6^6 should be independent of pressure. The pressure dependence of these ratios means that isotropic hydrostatic pressure can influence the local symmetry of

the coordination ion by changing the angles θ_L and ϕ_L. We have not observed any simple correspondence between the hydrostatic pressure and positions of individual ions; however, the presence of non-cubic distortion induced by pressure is visible especially in the behaviour of B_2^0 and the ratio B_4^3/B_4^0. We have noticed that non-cubic contributions to the crystal field, measured as differences between the obtained quantities of B_4^3/B_4^0 and B_6^6/B_6^0 and their cubic values, increase with pressure, whereas changes in the values of B_2^0 and B_6^3/B_6^6 with pressure suggest a decrease of the non-cubic crystal-field contributions.

4. Configurational coordinate diagram and discussion of the relative intensity of the emission from the $^3P_0$ and $^1D_2$ states.

The configurational coordinate diagram of Pr^{3+}, which includes both the $4f^2$ electronic manifolds and the trapped exciton manifold, can be derived by considering the following Hamiltonian:

$$H = \frac{-\hbar^2\nabla^2}{2m} + V_{\mathrm{RE}}(\mathbf{r})|_{r<R} + V_{\mathrm{cr}}(\mathbf{r})|_{r>R} - \frac{e^2}{\varepsilon \cdot r}|_{r>R} + V_{\mathrm{latt}}(\Delta) \tag{11}$$

where $V_{\mathrm{RE}}(\mathbf{r})|_{r<R}$ is the local potential corresponding to the short-range potential of the Pr^{4+} system, $\frac{-e^2}{r\varepsilon}$, where ε is the dielectric constant of the material, is the Coulomb potential of the Pr^{4+} ion replacing the triply ionized lattice ion, and $V_{\mathrm{cr}}(\mathbf{r})|_{r>R}$ is the lattice periodic potential. The lattice relaxation potential, $V_{\mathrm{latt}}(\Delta)$, describes the short-distance reaction of the lattice on the ionization of Pr from Pr^{3+} to Pr^{4+}. Labels $r > R$ and $r < R$ mean that the potential is definite outside and inside the first configurational sphere, respectively; R is the distance between the Pr^{3+} ion and ligands (here we consider the average distance).

One can consider that in the localized states of the Pr^{3+} ion (the $4f^2$ electronic configuration) the system is described by free-ion wavefunctions φ_l, and small contributions from the lattice are considered as perturbations in the framework of crystal-field theory [42].

When we deal with Pr^{4+} an electron in the conduction band is attracted by the long-range Coulomb potential of the trapped hole. In the standard approach [43, 44] one obtains 'the shallow donor' or 'effective Rydberg' states below each minimum of each conduction band. The situation is described by a set of Schrödinger equations labelled with band number 'n':

$$\left(-\frac{1}{2}\sum_{\alpha\beta}\frac{1}{m^n_{\alpha\beta}}\frac{\partial}{\partial x_\alpha}\frac{\partial}{\partial x_\beta} - \frac{1}{\varepsilon \cdot r} + E_n(\mathbf{k}=\mathbf{k}_{\min})\right) F_s^n(\mathbf{r}) = \mathrm{E}_s F_s^n(\mathbf{r}) \tag{12}$$

where $F_s^n(\mathbf{r})$ is the envelope function which extends quite far outside the Pr^{4+} ion. $E_n(\mathbf{k} = \mathbf{k}_{\min})$ is the energy of the minimum of the conduction band and $\frac{1}{m^n_{\alpha\beta}}$ is a composition of the inverse of effective mass tensor. Usually it is sufficient to consider the lowest conduction band. The contribution from the local potential $V_{\mathrm{RE}}(\mathbf{r})|_{r<R}$ to the energy of the effective Rydberg states can be calculated by a perturbation approach [45, 46].

The lattice relaxation, $V_{\mathrm{latt}}(\Delta)$, additionally diminishes the energy of the Pr^{3+} trapped exciton and shifts the respective electronic manifold in configurational space with respect to the $4f^2$ electronic manifolds of Pr^{2+} by Δ.

Since the lattice response on the Coulomb potential of Pr^{4+} (trapped hole) has already been included by the lattice polarization effect and described by the dielectric constant ε, the most important contribution to the lattice relaxation we have to consider here results from the local distortion of the lattice. One can consider this distortion as the compression of the quantum well formed by the central ions and ligands, resulting from the decrease of the number of electrons in the well system. Changes in energy result from a change in the kinetic energy of

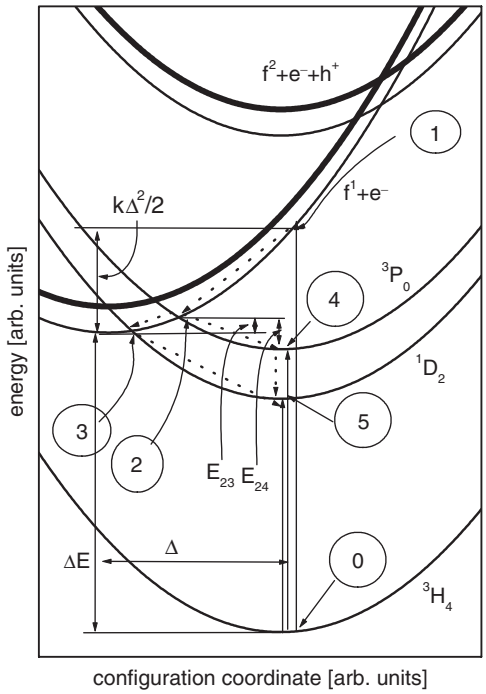

Figure 6. Configurational coordinate diagram of the $LiTaO_3:Pr^{3+}$ system.

the localized electron system. Considering that the size of the well is proportional to R one obtains a value of the kinetic energy of a single electron at the Fermi level in the well equal to $\frac{C}{R^2}$, where the constant C depends on the depth of the well and the number of electrons. Thus after removing a single electron one obtains the value of the lattice relaxation energy as a minimum of the following function:

$$V_{\text{latt}}(\Delta) = -\frac{C}{[R+\Delta]^2} + \frac{k\Delta^2}{2}. \tag{13}$$

The second term of equation (13) represents the elastic energy of the distorted system, where k is the elastic constant. The actual shift Δ can be calculated by minimalization of (13) with respect to Δ. Under the assumption that $\frac{\Delta}{R} \ll 1$, one obtains:

$$\Delta = -\frac{2C}{kR^3}. \tag{14}$$

Thus finally one obtains

$$V_{\text{latt}}(R) = -\frac{k}{2}\Delta^2 - \frac{C}{R^2} = -\frac{2C^2}{kR^6} - \frac{C}{R^2}. \tag{15}$$

Considering the above discussion one can represent the energetic structure of the Pr^{3+} ion using the configurational coordinate diagram presented in figure 6. In the diagram bold and thin curves labelled $f^2 + e^- + h^+$ correspond to the free electron and free hole, and free exciton state, respectively, for the case when the Pr^{3+} ion is in the ground state. Bold and thin curves labelled $f^1 + e^-$ correspond to a hole trapped at the Pr^{3+} ion (it is Pr^{4+}) and an electron in the conduction band, and trapped exciton, respectively. The localized states of the Pr^{3+} ion are labelled using the usual labels.

One can discuss why the trapped exciton can be formed by a hole localized at Pr^{3+} and an electron outside the ion. Actually the localization of an electron at the oxygen vacancy near Pr^{3+} is possible; however, it is difficult to find the mechanism that creates the oxygen vacancy near each praseodymium and then fills them with oxygen when the trapped exciton recombines through the $^1D_2$ or $^3P_0$ state of Pr^{3+}. The mechanism of lattice relaxation that is proposed here suggests the delocalization of the electron outside the Pr^{4+} ion but not at the particular neighbouring oxygen ion.

One notices that to ensure the stabilization of lattice relaxation we need only to remove the electron from the quantum well. In the effective mass approximation the envelope wavefunctions are the hydrogen-like $F_{nlm_l}(\mathbf{r})$ and they are labelled by hydrogen-like quantum numbers n, l, m_l [43, 44]. The probability of finding an electron inside the well is $\int_{r<R} F^*_{nlm_l}(\mathbf{r}) F_{nlm_l}(\mathbf{r})\,\mathrm{d}\mathbf{r}$, and $F_{nlm_l}(\mathbf{r})$ is proportional to $[\frac{2r}{na^*}]^l \exp[\frac{-r}{na^*}]$, where $a^* = 0.529\frac{\varepsilon}{m^*}$ Å is the effective Bohr radius (m^* is the effective mass). Since the effective mass is usually smaller than 1 and the dielectric constant is much larger than 1, the value of $\int_{r<R} F^*_{nlm_l}(\mathbf{r}) F_{nlm_l}(\mathbf{r})\,\mathrm{d}\mathbf{r}$ is rather small and can be negligible when $l > 0$ since it is proportional to r^l. In the case of $l = 0$ the probability of finding an electron cannot be negligible, and we have significant probability of exciton recombination. Thus one can conclude that the electron that forms the Pr^{3+} trapped exciton should be characterized by an orbital momentum quantum number larger than 0.

One can use the configurational coordinate diagram presented in figure 6 to analyse the pressure dependence of photoluminescence spectra. It is reasonable to assume that at ambient pressure the energies of the excited states of the Pr^{3+} that contribute to the emission, $^1D_2$ and $^3P_0$, are lower than the energy of the Pr^{3+} trapped exciton state. In figure 6 labels 0, 1, 2, 3, 4 and 5 correspond to the points on the diagram that are important for understanding the deexcitation kinetics.

Emission spectra of the $LiTaO_3$:Pr^{3+} system excited directly to the ^3P_J states (the respective transition is indicated in figure 6 by the solid arrow $0 \rightarrow 4$) are reported in [19]. According to [19], the emission band related to the $^3P_0 \rightarrow {}^3H_4$ transition is much stronger than that of $^1D_2 \rightarrow {}^3H_4$, and dominates in the spectrum. In our case when we excite the system though the excitation to the trapped exciton state (the respective transition is indicated in figure 6 by the solid arrow $0 \rightarrow 1$) the emission related to the $^1D_2 \rightarrow {}^3H_4$ transition is stronger than that of $^3P_0 \rightarrow {}^3H_4$ for all pressures and temperatures.

One considers that under continuous excitation the intensity of the luminescence related to the $^3P_0 \rightarrow {}^3H_4$ and $^1D_2 \rightarrow {}^3H_4$ transitions is proportional to the population of the $^3P_0$ and $^1D_2$ states, respectively, multiplied by the probability of the respective radiative processes. The quantities that depend on the excitation energy are population numbers. Thus under direct excitation to the ^3P_J state the luminescence due to the $^3P_0 \rightarrow {}^3H_4$ transition is larger than that of $^1D_2 \rightarrow {}^3H_4$ due the fact that nonradiative transitions $^3P_0 \rightarrow {}^1D_2$ (in figure 6 indicated with the dashed arrow $4 \rightarrow 5$) is less probable than the direct $^3P_0 \rightarrow {}^3H_4$ radiative process, and therefore the population of the $^1D_2$ state is smaller than that of $^3P_0$. Since the energy of the trapped exciton is greater than the energy of the $^3P_0$ state the deexcitation of the $^3P_0$ state through the trapped exciton is negligible for energetic reasons.

On the other hand, after excitation of the system to the trapped exciton state (indicated in figure 6 with the solid arrow $0 \rightarrow 1$) the lattice relaxes and the system transforms nonradiatively to points 2 and 3. Then the final metastable states are $^3P_0$, indicated as 4, or $^1D_2$, indicated as 5. One notices that the system reach the $^3P_0$ and $^1D_2$ states through the deexcitation pathways indicated by dashed arrows: $1 \rightarrow 2 \rightarrow 4$ and $1 \rightarrow 2 \rightarrow 3 \rightarrow 5$, respectively. The experimental effect of damping of the $^3P_0 \rightarrow {}^3H_4$ emission when the system is excited to the

trapped exciton state means that pathway $1 \rightarrow 2 \rightarrow 3 \rightarrow 5$ is more probable than $1 \rightarrow 2 \rightarrow 4$. In this consideration we have omitted the radiative recombination of the trapped exciton state, which is not observed experimentally.

One notices that after excitation $0 \rightarrow 1$ the system always relaxes to the point '2', and when the system reaches point '3' the only relaxation pathway is $3 \rightarrow 5$. Thus crucial for consideration of the deexcitation processes is the relation between the probabilities of nonradiative processes p_{23} and p_{24} that describe the $2 \rightarrow 3$ and $2 \rightarrow 4$ transitions, respectively, and are responsible for the depopulation of point 2. Probability p_{23} describes the intraconfigurational relaxation and it is proportional to the energy of crossing point 2 with respect to the minimum energy of the adiabatic potential representing the trapped exciton state (curve labelled as $f^1 + e^-$) [47]. This energy is indicated in figure 6 as E_{23}. Probability p_{24} describes the interconfigurational transitions [47], and depends on the transition moment that mixes electronic parts of the wavefunctions of the initial and final states and on the overlap integrals of the respective vibronic wavefunctions [48]. Our experimental results yield that $p_{23} > p_{24}$, at all considered pressures and temperatures. The weak probability of the interconfigurational transition p_{24} can be related to the fact that the ground state of the trapped exciton is a spin singlet and therefore is weakly mixed with the electronic wavefunctions of the ^3P_J states.

In figure 5 it is seen that at ambient temperature the intensity of the $^3P_0 \rightarrow {}^3H_4$ transition is smaller than at 20 K. This means that an increase in temperature diminishes the probability p_{24}. Actually this probability should be considered as temperature dependent due to thermal activation of the $4 \rightarrow 2 \rightarrow 3 \rightarrow 5$ nonradiative pathway. Assuming that the $3 \rightarrow 5$ nonradiative transition takes place between states of the same spin we can consider that the occupation number of point 3 is always small and therefore actual metastable states are always $^3P_0$ and $^1D_2$. Finally the $4 \rightarrow 2 \rightarrow 3 \rightarrow 5$ process is controlled by the difference between energies of points 2 and 4 labelled in figure 6 by E_{24}, which depends on pressure. One notices that

$$p_{24}(p) = \frac{p_{24}^0}{1 + \exp\left[-\frac{E_{24}(p)}{k_B T}\right]}. \tag{16}$$

Energy $E_{24}(p)$ decreases with pressure and therefore for high pressure p_{24} becomes independent of temperature for the available temperature range, as already observed in figure 5 above 100 kbar.

One notices that the ratio of the emission intensities originated at $^3P_0$ and $^1D_2$ is proportional to $\frac{p_{24}}{p_{23}}$. When we consider that similarly to the case of $LiNbO_3:Pr^{3+}$ in $LiTaO_3:Pr^{3+}$ pressure diminishes the energy of the trapped exciton state ΔE pressure caused damping of the $^3P_0 \rightarrow {}^3H_4$ emission is related also to increase of the probability p_{23} resulted from increase of energy E_{23}. For higher pressure it is possible that the energy of the trapped exciton can be smaller than the energy of the $^3P_0$ state as it is in the case of $LiNbO_3:Pr^{3+}$ [31].

5. Conclusions

The paper is devoted to high-pressure photoluminescence of the $LiTaO_3:Pr^{3+}$ system. We have presented the spectra obtained for the pressure range from ambient to 250 kbar at 20 K and ambient temperature. One has noticed that pressure causes a red shift of all spectral lines representing the f–f transitions. We have analysed the f–f luminescence spectra using the standard crystal-field approach. It has been found that the pressure shifts of the emission lines are mostly related to the changes in the F^2 Racach integral and the spin–orbit coupling.

We have noticed the pressure damping of the $^3P_0 \rightarrow {}^3H_4$ luminescence that has been attributed to the diminishing energy of the Pr^{3+} trapped exciton and nonradiative depopulation

of the $^3P_0$ by transfer of the excitation energy to the praseodymium trapped exciton. To analyse the dependence of the relative intensities of the $^3P_0 \rightarrow {}^3H_4$ and the $^1D_2 \rightarrow {}^3H_4$ transitions on excitation wavelength and pressure we have considered the model of a trapped exciton, where a hole has been localized at Pr^{3+} and an electron was bound by a Coulomb potential of Pr^{4+} at the effective mass shallow Rydberg states. The model was presented in the form of a configurational coordinate diagram. It has been found that an additional interaction that diminishes the energy of the trapped exciton is related to lattice relaxation. We have estimated this energy, as well as the amount of lattice distortion considering the lattice relaxation as the response of an elastic quantum well, formed by Pr and ligands, on the reduction of the number of f electrons of Pr from 2 to 1. The formulae obtained relate this energy and lattice distortion to the size of the PrO_6 system (see relations (14) and (15)). Since pressure compress the crystal, both the lattice relaxation energy and the amount of lattice distortion should increase with pressure. As the result we have a pressure-induced decrease of the energy of the Pr^{3+} trapped exciton state. This effect has already been observed in Pr^{3+}-doped $LiNbO_3$ [31].

In the framework of our approach we have predicted that an electron at the trapped exciton state should be described by a momentum quantum number $l > 0$.

Acknowledgment

The research presented in this paper has been supported by the Polish State Committee for Scientific Research by grant no. 2P03 B057 23.

References

[1] Matthias B T and Remika J P 1949 *Phys. Rev.* **76** 1886
[2] Inbar I and Cohen R E 1996 *Phys. Rev.* B **53** 1193
[3] Miller R C and Nordland W A 1970 *Phys. Rev.* B **2** 4896
[4] Tangonan G L, Barnoski M K, Lotspeich J F and Lee A 1977 *Appl. Phys. Lett.* **30** 238
[5] Amin J, Dussardier B, Schweizer T and Hempstead M 1996 *J. Lumin.* **69** 17
[6] Nunez L and Cusso F 1993 *J. Phys.: Condens. Matter* **5** 53001
[7] Łuzyński Z, Łukasiewicz T, Pracka I, Surma B and Malinowski M 1995 *J. Appl. Spectrosc.* **62** 66
[8] Lorenzo A, Bausá L E, Sanz J A and García-Solé J 1996 *J. Phys.: Condens. Matter* **8** 5781
[9] Loro H, Voda M, Jaque F, Muñoz-Santiste J E and Garcia-Sole J 1995 *J. Appl. Phys.* **77** 5929
[10] Lorenzo A, Camarillo E, Murrieta H S, Alvarez E, Caldino V G, Hernandez A, Voda M, Jaque F and Garcia-Sole J 1996 *Opt. Mater.* **5** 251
[11] Malinowski M, Miziak P, Piramidowicz R, Pracka I, Łukasiewicz T, Surma B, Kaczmarek S, Kopczyński K and Mierczyk Z 1996 *Acta Phys. Pol.* **90** 181
[12] Lorenzo A, Bausa L E and Gacia-Sole J 1995 *Phys. Rev.* B **51** 16643
[13] Piramidowicz R, Pracka I, Woliński W and Malinowski M 2000 *J. Phys.: Condens. Matter* **12** 709
[14] Thiemann O, Donnerberg H, Wohlecke M and Shirmer O F 1994 *Phys. Rev.* B **49** 5845
[15] Garcia-Sole J, Lou L, Monteil A, Boulon G, Lecocq S, Vergara I, Camarillo E and Cochet-Muchy D 1993 *Eur. J. Solid State Inorg. Chem.* **30** 1049
[16] Abedin K S, Sato M, Ito H, Maeda T, Schimamura K and Fukuda T 1995 *J. Appl. Phys.* **78** 691
[17] Wu X, Shong M S, Chen X, Meng X and Feng D 1994 *Appl. Phys. Lett.* **65** 1088
[18] Nikl M, Morlotti R, Margo C and Bracco R 1996 *J. Appl. Phys.* **79** 2853
[19] Sokólska I, Ryba-Romanowski W, Gołąb S, Łukasiewicz T and Świrkowicz M 1997 *J. Phys.: Condens. Matter* **9** 5217
[20] Vink A P, Dorenbos P and van Eijk C W E 2002 *Phys. Rev.* B **66** 075118
[21] Vink A P, van der Kolk E, Dorenbos P and van Eijk C W E 2002 *J. Alloys Compounds* **341** 338
[22] Dorenbos P 2000 *J. Lumin.* **91** 91
[23] van der Kolk E, Dorenbos P, Vink A P, Perego R C, van Eijk C W E and Lakshmanan A R 2004 *Phys. Rev.* B **64** 195129

[24] Rodnyi P A, Mikhrin S B, Dorenbos P, van der Kolk E, van Eijk C W E, Vink A P and Avanesov A G 2002 *Opt. Commun.* **204** 237
[25] van der Kolk E, Dorenbos P and van Eijk C W E 2001 *Opt. Commun.* **197** 317
[26] Vink A P, Dorenbos P and van Eijk C W E 2003 *J. Solid State Chem.* **171** 308
[27] Lorenzo A, Jaffrezic H, Roux B, Boulon G, Bausá L E and García Solé J 1995 *Phys. Rev.* B **52** 6278
[28] Heaton R A and Lin C C 1982 *Phys. Rev.* B **25** 3538
[29] Le Masson N J M, Vink A P, Dorenbos P, Bos A J J, van Eijk C W E and Chaminade J P 2003 *J. Lumin.* **101** 175
[30] Gryk W, Kukliński B, Grinberg M and Malinowski M 2004 *J. Alloys Compounds* **380** 230
[31] Gryk W, Dyl D, Grinberg M and Malinowski M 2005 *Phys. Status Solidi* c **2** 188
[32] Koepke Cz, Wisniewski K, Dyl D, Grinberg M and Malinowski M 2005 *Opt. Mater.* at press
[33] Judd B R and Crosswhite H 1984 *J. Opt. Soc. Am.* B **1** 255
[34] Judd B R 1963 *Operator Techniques in Atomic Spectroscopy* (New York: McGraw-Hill)
[35] Crosswhite H M and Crosswhite H 1984 *J. Opt. Soc. Am.* B **1** 246
[36] Muñoz-Santiuste J E, Lorenzo A, Bausá L E and García Solé J 1998 *J. Phys.: Condens. Matter* **10** 7653
[37] Görller-Warland Ch and Binnemans K 1996 *Handbook on the Physics of Rare Earth* vol 23 (Amsterdam: Elsevier Science B.V) p 121
[38] Newman D J and Ng B 2000 *Crystal Field Handbook* (Cambridge: Cambridge University Press)
[39] Carnall W T, Goodman G L, Rajnak K and Rana R S 1989 *J. Chem. Phys.* **90** 3443
[40] Morrison C A and Leavitt R P 1981 *J. Chem. Phys.* **74** 25
[41] Morrison C A, Leavitt R P and Wortman D E 1980 *J. Chem. Phys.* **73** 2580
[42] Henderson B and Imbusch G F 1989 *Optical Spectroscopy of Inorganic Solids* (Oxford: Clarendon)
[43] Luttinger J M and Kohn W 1955 *Phys. Rev.* **97** 869
[44] Kohn W 1957 *Solid State Phys.* **5** 257
[45] Pantelides S T and Sah C T 1974 *Phys. Rev.* B **10** 638
[46] Grinberg M 1986 *Phys. Status Solidi* **138** 275
[47] Grinberg M and Mandelis A 1994 *Phys. Rev.* B **49** 12496
[48] Grinberg M, Mandelis A and Fjeldsted K 1993 *Phys. Rev.* B **48** 5935